

Transparent Boundary Conditions for Elastic Anisotropic VTI Media: Axially Symmetric Case

Olga Podgornova*

Schlumberger Moscow Research, 13, Pudovkina, 119285, Russia.

Received 22 December 2009; Accepted (in revised version) 5 May 2011

Available online 24 October 2011

Abstract. Transparent boundary conditions (TBCs) for anisotropic vertical transverse isotropic VTI medium are formulated for the axially symmetric case. The high accuracy of the derived TBCs and their long-time stability are demonstrated in numerical experiments. The TBCs are represented in terms of the vertical component of the velocity vector and tangential component of the stress tensor that facilitates the easy implementation of the boundary condition into the finite-difference staggered-grid scheme.

AMS subject classifications: 65M99, 35L05, 30E10, 74E10, 74B05

Key words: Nonreflecting boundary conditions, anisotropy, elastodynamics.

1 Introduction

Numerical modeling of wave propagation in an unbounded physical domain is usually performed in a finite computational domain with nonreflecting boundary conditions applied on its boundary; these conditions should guarantee low (ideally no) spurious reflected waves at the boundary. In the context of acoustic, elastic, and electromagnetic wave propagation, many publications could be mentioned, but we refer just to the reviews [4, 11], see also the references therein.

Formulation of accurate, stable, and computationally efficient nonreflecting conditions in the case of elastic *anisotropic* media has become a hot topic of research in recent years, basically after Becache et al. [2] demonstrated that although perfectly matched layer (PML) [3] is good for isotropic media, it may be unstable for anisotropic media. Several interesting approaches for anisotropic elastic problems, such as a multiaxial PML [6] and truncation method on a base of optimal grids [5], have been proposed just recently. Here, we address the problem of constructing nonreflecting boundary conditions for anisotropic elastic media in the framework of transparent boundary conditions, [1, 7, 8].

*Corresponding author. *Email address:* opodgornova@s1b.com (O. Podgornova)

For isotropic media, transparent boundary conditions (TBCs) have been obtained for many problems, including acoustic, linearized Euler, and Maxwell equations. Typically TBCs are described by an integrodifferential operator represented by a sum of local terms, like time and spatial derivatives, and a nonlocal term (an integral of convolutional type). In simple cases, e.g. a wave equation in homogeneous media and the boundary of a simple shape (planar, spherical, and cylindrical), either the convolutional kernel itself or its Laplace transform is obtained analytically. The alternative for the cases when the analytical formulas are unknown is the recently proposed quasi-analytical TBCs [9], where the Laplace transform of the kernel is calculated numerically for anisotropic vertically transverse isotropic (VTI) media for the axially symmetric case, (r,z) -geometry. However media with smooth z -dependent parameters in the exterior domain are allowed in the approach [9] and it is very computationally expensive.

In this work we obtain analytical formulas of TBC for the particular, but practically important case of axially symmetric anisotropic elastic VTI media. The derivation of TBC for this case is a more technically sophisticated task than that of TBCs for an acoustic scalar equation [1]. Fortunately, in spite of complicated intermediate formulas, the final form of TBC is relatively simple. We restrict here to the case of a cylindrical boundary and homogeneous media in the exterior domain, though any arbitrary complex medium is allowed in the interior domain. Similar to other cases (excluding the 1D wave equation), TBC is described with the operator that contains both local and non-local terms in time and space. The local term can be used for the problems that require moderate accuracy. To achieve higher accuracy we should include the non-local term, which is approximated via the convolution with a sum of exponentials according to [1, 8] for the efficient numerical implementation.

The rest of the paper is organized as follows. We start with the problem formulation in Section 2. Section 3 is devoted to the derivation of analytical formulas for TBC. Approximation of the boundary condition is discussed in Section 4, and discretization for a finite-difference staggered-grid scheme is outlined briefly in Section 5. The numerical experiments and their results are described in Section 6.

2 Problem formulation

We consider a stress-velocity formulation of the elastodynamics equations for the rotationally symmetric case in anisotropic VTI media where the equations of motion are

$$\rho \frac{\partial u_r}{\partial t} = \frac{\partial \sigma_{rr}}{\partial r} + \frac{\sigma_{rr}}{r} - \frac{\sigma_{\varphi\varphi}}{r} + \frac{\partial \sigma_{rz}}{\partial z} + \rho S_r, \quad (2.1a)$$

$$\rho \frac{\partial u_z}{\partial t} = \frac{\partial \sigma_{rz}}{\partial r} + \frac{\sigma_{rz}}{r} + \frac{\partial \sigma_{zz}}{\partial z} + \rho S_z, \quad (2.1b)$$

and the Hooke's law is

$$\frac{\partial \sigma_{rr}}{\partial t} = A_{11} \frac{\partial u_r}{\partial r} + A_{12} \frac{u_r}{r} + A_{13} \frac{\partial u_z}{\partial z} + S_{rr}, \tag{2.2a}$$

$$\frac{\partial \sigma_{\varphi\varphi}}{\partial t} = A_{12} \frac{\partial u_r}{\partial r} + A_{11} \frac{u_r}{r} + A_{13} \frac{\partial u_z}{\partial z} + S_{\varphi\varphi}, \tag{2.2b}$$

$$\frac{\partial \sigma_{zz}}{\partial t} = A_{13} \frac{\partial u_r}{\partial r} + A_{13} \frac{u_r}{r} + A_{33} \frac{\partial u_z}{\partial z} + S_{zz}, \tag{2.2c}$$

$$\frac{\partial \sigma_{rz}}{\partial t} = A_{44} \left(\frac{\partial u_r}{\partial z} + \frac{\partial u_z}{\partial r} \right) + S_{rz}. \tag{2.2d}$$

Here (u_r, u_z) and $(\sigma_{rr}, \sigma_{\varphi\varphi}, \sigma_{zz}, \sigma_{rz})$ are the components of the velocity vector and stress tensor in (r, z) -coordinates respectively; ρ is the density; $A_{11}, A_{33}, A_{44}, A_{12}, A_{13}$ are the parameters of the anisotropic medium; $S_r, S_z, S_{rr}, S_{\varphi\varphi}, S_{zz}, S_{rz}$ are the components of the source term.

We consider the wave process in the infinite strip $(r, z) \in [0, +\infty) \times [Z_{bot}, Z_{top}]$ with zero initial conditions and simple boundary data on the top and bottom boundaries $z = Z_{top}$ and $z = Z_{bot}$

$$u_z = 0, \quad \sigma_{rz} = 0. \tag{2.3}$$

The computational domain is a rectangular $[0, R_\Gamma] \times (Z_{bot}, Z_{top})$ and on the right boundary $r = R_\Gamma$ the transparent boundary condition is set. The outgoing waves leave thus the domain without reflection from the boundary. We assume that source term functions are equal to zero and that density and anisotropic parameters are constants outside the computational domain ($r > R_\Gamma$); an arbitrary source term and anisotropic media are allowed inside the computational domain ($r < R_\Gamma$). The geometry of the problem is depicted at Fig. 1.

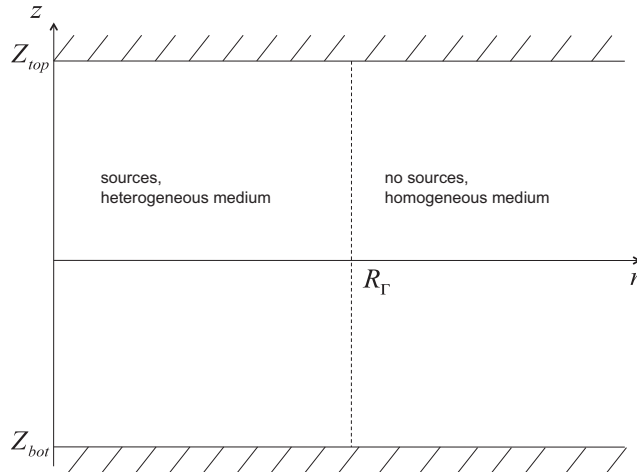


Figure 1: Schematic view of the geometry of the TBCs problem.

3 Transparent boundary condition

We derive the relation between the solution and its normal derivative defined by a Fourier transformation along the boundary and a Laplace transformation in time. Then we transform the relation back into the physical space.

We formulate the boundary condition as equations for the radial component u_r of the velocity field and the tangential component σ_{rz} of the stress tensor. Such a formulation is very convenient for a finite-difference staggered-grid discretization as we show further. The formulation of the boundary condition as equations for radial and vertical components of the displacements can be obtained as well, e.g., quasi-analytical TBCs [9].

3.1 A TBC in the spectral space

We apply a Fourier transformation \mathcal{F} along the variable z and a Laplace transformation \mathcal{L} along the variable t

$$\bar{g}(t, r, l) = \mathcal{F}[g(t, r, z)], \quad \hat{g}(s, r, l) = \mathcal{L}[\bar{g}(t, r, l)], \quad g = u_r, u_z, \sigma_{rr}, \sigma_{\varphi\varphi}, \sigma_{zz}, \sigma_{rz},$$

to the source-free equations (2.1) and (2.2) in a homogeneous medium. Here l and s are dual variables for z and t respectively. From the obtained system of ordinary differential equations with the parameters l and s we exclude components $u_z, \sigma_{rr}, \sigma_{\varphi\varphi}, \sigma_{zz}$; after some algebraic transformations, we obtain a second-order system for u_r and σ_{rz}

$$\frac{\partial^2}{\partial r^2} \begin{bmatrix} \hat{u}_r \\ \hat{\sigma}_{rz} \end{bmatrix} + \frac{1}{r} \frac{\partial}{\partial r} \begin{bmatrix} \hat{u}_r \\ \hat{\sigma}_{rz} \end{bmatrix} - \frac{1}{r^2} \begin{bmatrix} \hat{u}_r \\ \hat{\sigma}_{rz} \end{bmatrix} + M \begin{bmatrix} \hat{u}_r \\ \hat{\sigma}_{rz} \end{bmatrix} = 0, \quad (3.1)$$

where the matrix M is defined by

$$M = \begin{pmatrix} \frac{A_{13}}{A_{11}} l^2 - \frac{1}{A_{11}} \rho s^2 & i l s \left(\frac{A_{13}}{A_{11} A_{44}} + \frac{1}{A_{11}} \right) \\ \frac{i l}{s} \left(\left(-\frac{A_{13}^2}{A_{11}} + A_{33} \right) l^2 + \left(\frac{A_{13}}{A_{11}} + 1 \right) \rho s^2 \right) & \left(\frac{A_{13}^2}{A_{11} A_{44}} + \frac{A_{13}}{A_{11}} - \frac{A_{33}}{A_{44}} \right) l^2 - \frac{1}{A_{44}} \rho s^2 \end{pmatrix}.$$

Using the representation of the matrix M in terms of eigenvalues and eigenvectors, $M = T \cdot \text{diag}\{\kappa_+^2, \kappa_-^2\} \cdot T^{-1}$, we split the system (3.1) into two independent equations

$$\frac{\partial^2 v_{\pm}}{\partial r^2} + \frac{1}{r} \frac{\partial v_{\pm}}{\partial r} - \left(\frac{1}{r^2} + \kappa_{\pm}^2 \right) v_{\pm} = 0 \quad (3.2)$$

with

$$\begin{bmatrix} v_+ \\ v_- \end{bmatrix} = T^{-1} \begin{bmatrix} \hat{u}_r \\ \hat{\sigma}_{rz} \end{bmatrix}.$$

The solutions to (3.2), that decay for $r \rightarrow +\infty$, are given by

$$v_{\pm} = C(l, s) K_1(\kappa_{\pm} r), \quad (3.3)$$

where K_1 is a 1st order Macdonald function corresponding to a modified Bessel function of the second kind, and $C(l,s)$ is a coefficient, independent of r . Using (3.3), we obtain a relation between v_{\pm} and its normal derivative $\partial v_{\pm} / \partial r$,

$$\frac{\partial v_{\pm}}{\partial r} = \kappa_{\pm} \frac{K_1'(\kappa_{\pm} r)}{K_1(\kappa_{\pm} r)} v_{\pm}.$$

Transferring back to the functions \hat{u}_r and $\hat{\sigma}_{rz}$, we get

$$\frac{\partial}{\partial r} \begin{bmatrix} \hat{u}_r \\ \hat{\sigma}_{rz} \end{bmatrix} = \hat{P}(s,l) \begin{bmatrix} \hat{u}_r \\ \hat{\sigma}_{rz} \end{bmatrix}, \tag{3.4}$$

where

$$\hat{P} = T \cdot \text{diag} \left\{ \kappa_+ \frac{K_1'(\kappa_+ r)}{K_1(\kappa_+ r)}, \kappa_- \frac{K_1'(\kappa_- r)}{K_1(\kappa_- r)} \right\} \cdot T^{-1}. \tag{3.5}$$

The transparent boundary condition in the spectral space is then defined by Eq. (3.4), which is a relation between \hat{u}_r , $\hat{\sigma}_{rz}$ and their normal derivatives $\partial \hat{u}_r / \partial r$, $\partial \hat{\sigma}_{rz} / \partial r$.

We calculate the eigenvalues κ_+^2 , κ_-^2 , the matrix T and we obtain \hat{P} by Eq. (3.5). After some algebraic calculations, we get

$$\hat{P} = \frac{\chi_- - \chi_+}{2\sqrt{\xi l^4 + \eta \rho l^2 s^2 + \zeta \rho^2 s^4}} P_0 + \frac{(\chi_+ + \chi_-)}{2} \begin{pmatrix} 1 & 0 \\ 0 & 1 \end{pmatrix}, \tag{3.6}$$

where

$$P_0 = \begin{pmatrix} a_0 l^2 + a_2 \rho s^2 & ib_1 s l \\ ic_{-1} l^3 / s + ic_1 \rho s l & -a_0 l^2 - a_2 \rho s^2 \end{pmatrix},$$

and the scalar functions read as

$$\chi_{\pm} = \kappa_{\pm} K_1'(r\kappa_{\pm}) / K_1(r\kappa_{\pm})$$

with

$$\kappa_{\pm} = \sqrt{\alpha l^2 + \beta \rho s^2 \mp \sqrt{\xi l^4 + \eta \rho s^2 l^2 + \zeta \rho^2 s^4}}.$$

In the above formulas the parameters $a_0, a_2, b_1, c_1, c_{-1}, \alpha, \beta, \xi, \eta, \zeta$ depend on the elastic coefficients as follows:

$$\begin{aligned} a_0 &= \frac{A_{13}^2 - A_{11}A_{33}}{2A_{11}A_{44}}; & a_2 &= \frac{-A_{11} + A_{44}}{2A_{11}A_{44}}; & b_1 &= -\frac{A_{13} + A_{44}}{A_{11}A_{44}}; \\ c_1 &= \frac{A_{11} + A_{13}}{A_{11}}; & c_{-1} &= -2A_{44}a_0; & \alpha &= \frac{-A_{13}^2 - 2A_{13}A_{44} + A_{11}A_{33}}{2A_{11}A_{44}}; \\ \beta &= \frac{A_{11} + A_{44}}{2A_{11}A_{44}}; & \xi &= \alpha^2 - \frac{A_{33}}{A_{11}}; & \eta &= 2\alpha\beta - \frac{A_{33} + A_{44}}{A_{11}A_{44}}; & \zeta &= a_2^2. \end{aligned}$$

3.2 A TBC in the physical space

Before applying inverse Laplace and Fourier transformations, we represent the matrix (3.6) in the following form

$$\hat{P} = sQ_1 + \frac{1}{r}Q_0 + ilQ_2 + \hat{K}(s) + \frac{1}{s}Q_{-1}, \tag{3.7}$$

where we extract explicitly the asymptotic term at $s \rightarrow \infty$ and a singularity at $s = 0$.

We use symbolic algebra software to calculate matrices Q_0, Q_1, Q_2, Q_{-1} . The first three of them have a very compact form and depend only on media parameters

$$Q_1 = -\frac{\sqrt{\rho}}{\sqrt{A_{11}A_{44}}} \begin{pmatrix} \sqrt{A_{44}} & 0 \\ 0 & \sqrt{A_{11}} \end{pmatrix}, \quad Q_0 = -\frac{1}{2} \begin{pmatrix} 1 & 0 \\ 0 & 1 \end{pmatrix}, \tag{3.8a}$$

$$Q_2 = \frac{1}{\sqrt{\rho A_{11}A_{44}}(\sqrt{A_{11}} + \sqrt{A_{44}})} \begin{pmatrix} 0 & A_{13} + A_{44} \\ \rho A_{44}(A_{11} + A_{13}) & 0 \end{pmatrix}. \tag{3.8b}$$

Matrix Q_{-1} contains only one nonzero element

$$Q_{-1} = \begin{pmatrix} 0 & 0 \\ q & 0 \end{pmatrix},$$

$$q = -\frac{ic_{-1}l^3}{2\sqrt{\xi}|l|} \left(-\sqrt{-\alpha - \sqrt{\xi}} \frac{K_1'(r|l|\sqrt{-\alpha - \sqrt{\xi}})}{K_1(r|l|\sqrt{-\alpha - \sqrt{\xi}})} + \sqrt{-\alpha + \sqrt{\xi}} \frac{K_1'(r|l|\sqrt{-\alpha + \sqrt{\xi}})}{K_1(r|l|\sqrt{-\alpha + \sqrt{\xi}})} \right).$$

We calculate \hat{K} as

$$\hat{K}(s) = \hat{P} - sQ_1 - \frac{1}{r}Q_0 - ilQ_2 - \frac{1}{s}Q_{-1}. \tag{3.9}$$

Both the coefficient q and the matrix $\hat{K}(s)$ depend on media parameters, harmonic number l and the boundary position R_Γ ; elements of $\hat{K}(s)$ go to 0 as $s \rightarrow +\infty$.

After backward Fourier and Laplace transformations of (3.4) with \hat{P} represented as in (3.7), we obtain TBC in physical space as follows

$$Q_1 \frac{\partial}{\partial t} \begin{bmatrix} u_r \\ \sigma_{rz} \end{bmatrix} - \frac{\partial}{\partial r} \begin{bmatrix} u_r \\ \sigma_{rz} \end{bmatrix} + \frac{1}{r}Q_0 \begin{bmatrix} u_r \\ \sigma_{rz} \end{bmatrix} + Q_2 \frac{\partial}{\partial z} \begin{bmatrix} u_r \\ \sigma_{rz} \end{bmatrix} + \mathcal{F}^{-1} \bar{K} * \mathcal{F} \begin{bmatrix} u_r \\ \sigma_{rz} \end{bmatrix} + \mathcal{F}^{-1} Q_{-1} \mathcal{F} \int_0^t \begin{bmatrix} u_r \\ \sigma_{rz} \end{bmatrix} d\tau = 0. \tag{3.10}$$

The asterisk $*$ denotes convolution with respect to time

$$u * v = \int_0^t u(t - \tau)v(\tau) d\tau,$$

and convolutional kernel is $\bar{K}(t) = \mathcal{L}^{-1}[\hat{K}(s)]$.

In this work we check the stability of the TBC (3.10) on several numerical experiments that are described further; the rigour analysis of the stability should be done in the future.

4 Approximation of the TBC

The straightforward calculation of the first convolutional integral in (3.10) is a time and memory consuming procedure because all history of the solution on the boundary should be taken into account in the computations for each time t . Therefore to calculate the convolution, we construct a computationally efficient approximation based on recurrence formulas according to [1, 8]. In addition, the approximation is required anyway since the analytical expression of the convolutional kernel in time domain $\bar{K}(t)$ is unknown. We describe the main ideas of the algorithm below.

We approximate each element of the matrix $\hat{K}(s)$ by rational functions enforcing the constraint that all poles (P_{ij} is the number of poles) have negative real parts

$$\hat{K}_{ij}(s) \approx \sum_{p=1}^{P_{ij}} \frac{\alpha_{ij}^p}{s - \beta_{ij}^p}, \quad \operatorname{Re}(\beta_{ij}^p) < 0, \quad i, j = 1, 2. \quad (4.1)$$

Then the approximation of the inverse Laplace transform is a sum of decaying exponentials

$$\bar{K}_{ij}(t) \approx \sum_{p=1}^{P_{ij}} \alpha_{ij}^p e^{\beta_{ij}^p t}, \quad \operatorname{Re}(\beta_{ij}^p) < 0, \quad i, j = 1, 2, \quad (4.2)$$

and the convolutional integral in the TBC is approximated via a sum of convolutions with exponentials

$$\int_0^t \bar{K}_{ij}(t-\tau) g(\tau) \approx \sum_{p=1}^{P_{ij}} \alpha_{ij}^p \int_0^t g(\tau) e^{\beta_{ij}^p(t-\tau)} d\tau, \quad g = \bar{u}_r, \bar{\sigma}_{rz}. \quad (4.3)$$

The advantage of using approximation (4.3) lies in the fact that a convolution with an exponential can be calculated by recurrence formulas

$$I_{ij}^p(t) = \int_0^t g(\tau) e^{\beta_{ij}^p(t-\tau)} d\tau, \quad p = 1, \dots, P_{ij}, \quad (4.4a)$$

$$I_{ij}^p(t+\Delta t) = e^{\beta_{ij}^p \Delta t} I_{ij}^p(t) + \int_0^{\Delta t} g(t+\tau) e^{\beta_{ij}^p(\Delta t-\tau)} d\tau. \quad (4.4b)$$

We have observed that in many cases, several tens of the exponentials are enough to approximate the convolutional kernel on several thousand time steps, i.e., Eqs. (4.3) and (4.4) perform very well. We refer the reader to [1] for a discussion on the influence of the number of the exponentials on accuracy of the solution for a case of scalar wave equation.

The second non-local integral term in the TBC is, actually, a convolution with zero exponential, therefore it is treated in the same way.

In our numerical experiments, instead of constructing rational approximations of the four elements of the matrix $\hat{K}(s)$ we construct approximations of two scalar functions

$$f_1(s) = \frac{\chi_- - \chi_+}{\sqrt{\zeta l^4 + \eta \rho l^2 s^2 + \zeta \rho^2 s^4}}, \quad (4.5a)$$

$$f_2(s) = \chi_+ + \chi_- + \sqrt{\rho} \left(\frac{1}{\sqrt{A_{11}}} + \frac{1}{\sqrt{A_{44}}} \right) s + \frac{1}{r}, \quad (4.5b)$$

where both $f_1(s) \rightarrow 0$, $f_2(s) \rightarrow 0$ when $s \rightarrow +\infty$; functions χ_{\pm} , parameters ζ , η , ζ are defined in Section 3.1, l corresponds to the Fourier harmonic. Rational approximations of $\hat{K}_{ij}(s)$ are then obtained from (3.6), (3.9), and (4.5).

To improve the efficiency of the TBC we also omit the convolutional term for a high-frequency Fourier harmonics. If no Fourier harmonics are taken into account in convolution, Eq. (3.10) reduces then to computationally cheap but not very accurate local boundary conditions.

Rational approximations can be obtained by one of the two algorithms, that have been used previously for the approximation of the convolutional kernels for the wave equation: the iterative algorithm [1], and the algorithm based on the Pade-Chebyshev approximations [8]. Here we apply the algorithm suggested in [8]; we adjust the number of exponentials empirically while estimating the accuracy of the approximation a posteriori. Typically, the larger the number of exponentials is, the better the accuracy is. Here our goal is to validate the robustness of the TBC (3.10); further work is required to optimize the number of the exponentials and to create a robust algorithm with guaranteed accuracy.

5 Discretization of the TBC

Here we describe the numerical discretization and implementation of the TBC (3.10) in a second order finite-difference staggered-grid scheme [12] for elastodynamics equations (2.1), (2.2). The stencil of the scheme is shown in Fig. 2 (left); the components of the velocity vector and stress tensor are defined in the staggered spatial points. The integer time steps t_p correspond to the time moments where velocities are defined, and half integer time steps $t_{p+1/2}$ correspond to the time moments where the stresses are defined.

We associate the right boundary of the computational domain, $r = r_M$, to a vertical grid line where u_r and σ_{rz} are defined. The discretized TBC are used to update u_r and σ_{rz} at $r = r_M$, while the other components of the solution are updated by the staggered-grid scheme. To get an update at the time steps $t = t_{p+1}$ and $t = t_{p+3/2}$, we approximate the first equation of (3.10) by central finite differences at the point $R_{\Gamma} = (r_{M-1} + r_M)/2$ and $t^{p+1/2}$. While discretizing the convolutional term the values of u_r at $(R_{\Gamma}, t^{p+1/2})$ are defined as a half sum of the values at (r_{M-1}, t^{p+1}) and (r_M, t^p) , see Fig. 2 (right). The second equation of (3.10) is approximated in a similar way at the point $R_{\Gamma} = (r_{M-1} + r_M)/2$ and t^{p+1} .

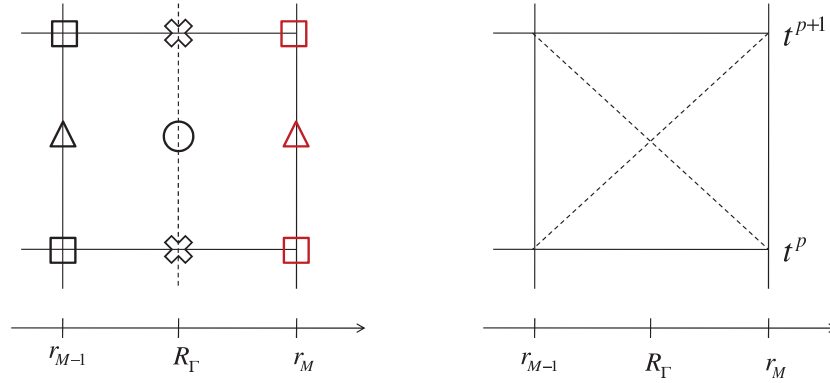


Figure 2: Schematic representation of the computational algorithm of finite-difference staggered-grid scheme coupled with the TBC. Left: cell adjoining the right boundary in (r, z) plane; triangles are for the points where u_r is defined, crosses for u_z , circles for σ_{rr} , $\sigma_{\phi\phi}$, σ_{zz} , rectangles for σ_{rz} ; black colored points are updated by Virieux scheme, red colored are updated by discretized TBCs. Right: (r, t) plane; stencil for time integration.

6 Numerical examples

In the first experiment, we study elastic waves generated by a point source in a homogeneous anisotropic medium for which PML is unstable. The medium parameters A_{11} , A_{12} , A_{13} , A_{33} , A_{44} are

$$A_{11} = \rho V_{P0}^2 (1 + 2\epsilon), \quad A_{12} = \rho V_{P0}^2 (1 + 2\epsilon) - 2\rho V_{S0}^2 (1 + 2\gamma),$$

$$A_{13} = \rho \sqrt{(V_{P0}^2 - V_{S0}^2)^2 + 2\delta V_{P0}^2 (V_{P0}^2 - V_{S0}^2)} - \rho V_{S0}^2, \quad A_{33} = \rho V_{P0}^2, \quad A_{44} = \rho V_{S0}^2,$$

where Thompsen parameters [10] are

$$\rho = 2.57, \quad V_{P0} = 4.449, \quad V_{S0} = 2.585, \quad \delta = 0.565, \quad \epsilon = 0.091, \quad \gamma = 0.046.$$

The computational domain is a rectangular $[0, R_\Gamma] \times [Z_{bot}, Z_{top}]$ elongated along z axis with $Z_{top} = -Z_{bot} = 5$ and $R_\Gamma = 0.3$. The TBC is applied at $r = R_\Gamma$. A point source is introduced at $(0, z_s)$ as a right hand side for the diagonal stress components in Eq. (2.2)

$$S_{rr} = S_{\phi\phi} = S_{zz} = \delta(r) \delta(z - z_s) R(t),$$

where

$$R(t) = \left(1 - 2\pi^2 \nu_0^2 (t - d)^2\right) e^{-\pi^2 \nu_0^2 (t - d)^2}$$

is the Ricker pulse with the central frequency $\nu_0 = 4$ and delay $d = 2/\nu_0$.

To estimate the accuracy of the TBC, we compute the solutions on three equidistant grids with different values of grid size h and measure the average relative error in two sets of the receivers. One set of 25 receivers is located close to the axis of symmetry at $r = 0.025$, the other is closer to the computational boundary, at $r = 0.25$. The lowest

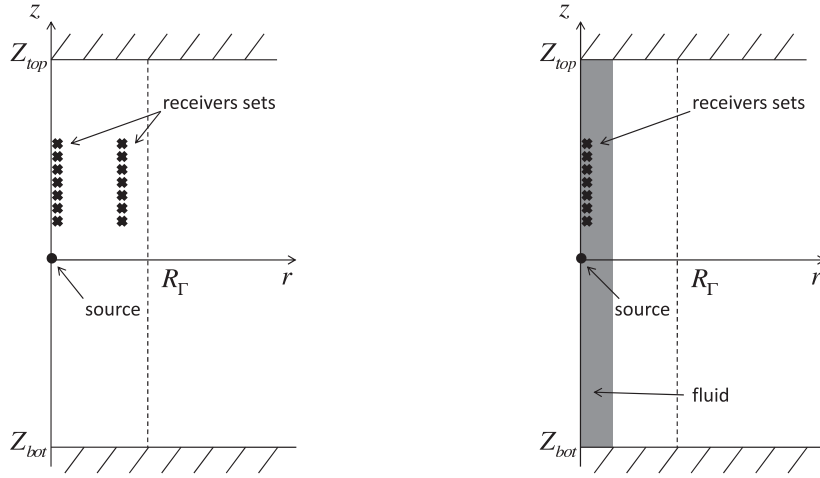


Figure 3: Schematic view of the numerical experiments geometry. Testcase for homogeneous medium (left). Testcase for wellbore with fluid (right). The ratio between width and height is not adjusted as computational domain is too narrow, $R_\Gamma / (Z_{top} - Z_{bot}) = 0.03$.

receiver in both sets has a vertical coordinate $z = 1.0$ and the gap between receivers is 0.1 in z direction. A schematic view of the geometry is shown in Fig. 3 (left).

Comparisons are made using results of computations on a large domain obtained by elongating the computational area along r . The right boundary of this large domain is very distant to R_Γ to guarantee that no reflections from the boundary are observed during the simulation time $T = 2.8$. In addition, we use a very fine grid on the large domain to compute what we call the reference solution.

We compute three kinds of relative errors on each grid: an approximation error ϵ_a , a TBC error ϵ_t , and a mixed error ϵ_{a+t} (i.e. a sum of the approximation and the TBC errors). These errors are defined as

$$\epsilon_a = \frac{\|U_h^{ext} - U^{ref}\|}{\|U^{ref}\|}, \quad \epsilon_t = \frac{\|U_h^{ext} - U_h^{tbc}\|}{\|U_h^{ext}\|}, \quad \epsilon_{a+t} = \frac{\|U_h^{tbc} - U^{ref}\|}{\|U^{ref}\|}.$$

Here $U = (u_r, u_z)^t$; U_h^{tbc} (resp. U_h^{ext}) is the solution computed on a grid with a mesh size h with the TBC (in the large domain); U^{ref} is the reference solution. The value of ϵ_a characterizes the error of the finite difference scheme; ϵ_t contains the error due to approximation and discretization of the TBC only; ϵ_{a+t} includes both the scheme and the TBC errors. The errors are defined as discrete analogs of L_∞ and L_2 norms in time.

In Tables 1 and 2 we present ϵ_a and $\epsilon_{t, n_{TBC}}$ as a function of the number of Fourier harmonics n_{TBC} used in the approximation of the convolution. The results reveal that the TBC error becomes less than the scheme error, i.e. $\epsilon_t < \epsilon_a$, if n_{TBC} is large enough (e.g. about 90 for $h = 0.01$, about 120 for $h = 0.005$). Fig. 4 shows the normalized solution in a particular receiver for a grid with $h = 0.01$. The difference between the solution with the TBC and the one calculated on the extended in r domain is barely visible. The

Table 1: Accuracy of the TBC compared to the numerical scheme accuracy for different grid size h , L_2 -norm.

	ϵ_a	$\epsilon_{t,80}$	$\epsilon_{t,90}$	$\epsilon_{t,94}$	$\epsilon_{t,96}$	$\epsilon_{t,100}$	$\epsilon_{t,120}$	$\epsilon_{t,140}$	$\epsilon_{t,200}$
h=0.01	4.2e-2	9.1e-2	4.3e-2	2.4e-2	1.9e-2	1.5e-2	1.4e-2	1.4e-2	1.4e-2
h=0.005	1.0e-2	8.6e-2	4.0e-2	2.1e-2	1.4e-2	5.8e-3	3.4e-3	3.4e-3	3.4e-3
h=0.003	3.8e-3	8.4e-2	4.0e-2	2.1e-2	1.4e-2	5.0e-3	1.3e-3	1.3e-3	1.3e-3

Table 2: Accuracy of the TBC compared to the numerical scheme accuracy for different grid size h , L_∞ -norm.

	ϵ_a	$\epsilon_{t,80}$	$\epsilon_{t,90}$	$\epsilon_{t,94}$	$\epsilon_{t,96}$	$\epsilon_{t,100}$	$\epsilon_{t,120}$	$\epsilon_{t,140}$	$\epsilon_{t,200}$
h=0.01	4.1e-2	8.3e-2	4.2e-2	2.4e-2	2.0e-2	1.7e-2	1.6e-2	1.6e-2	1.6e-2
h=0.005	1.0e-2	7.2e-2	4.0e-2	2.1e-2	1.4e-2	5.7e-3	4.0e-3	4.0e-3	4.0e-3
h=0.003	3.6e-3	6.8e-2	3.9e-2	2.1e-2	1.5e-2	4.4e-3	1.5e-3	1.4e-3	1.4e-3

stagnation of the error $\epsilon_{t,n_{TBC}}$ from a given n_{TBC} , depending on the grid size, is caused by the discretization error of the TBC equations (3.10).

For a fixed and big enough n_{TBC} , according to Tables 1, 2, the error decreases with the second order rate while the size of the grid decreases, and it corresponds to the second order accuracy of the TBC discretization. Actually, such a behavior demonstrates that the accuracy of the approximation of the convolutional kernel is satisfactory for the considered problem; otherwise, the error should stagnate with the decreasing grid size.

In fact, a test of this kind can be used for additional validation of the accuracy of the exponential approximations. In the current example, we achieve the accuracy better than 10^{-4} using 30-40 exponentials for each of the functions f_1, f_2 , see (4.5). We believe that our numbers are not optimal and can be reduced.

We demonstrate the time dependence of ϵ_a and ϵ_{a+t} for a mesh size $h = 0.01$ and $n_{TBC} = 100$ in Fig. 5. The value of the approximation error ϵ_a is negligible after $t = 2.4$. This is expected since, at that time, the major part of the solution leaves the region where the receivers are located. For times $t < 2.4$, the errors ϵ_a and ϵ_{a+t} are close to each other and that means the TBC doesn't corrupt the accuracy of the solution. The spurious reflections from the TBC come out at later time points. However the value of their amplitude is an order less than the scheme error and almost three orders less than the amplitude of the solution at earlier times; such a behavior of the errors (i.e. $\epsilon_t < \epsilon_a$) is observed for all experiments for large enough n_{TBC} .

In our long-time simulations with the TBC up to $T=20$ ($n_{TBC}=200$) we do not observe any instability. Fig. 5 (right) shows the norm of the solution up to $T = 4$; the amplitude of the spurious reflections due to the TBC is about 0.1%. We do not show the norm at the later time as, due to the periodicity of the problem in the vertical direction, the reflections from the top and bottom start arriving and the value of the norm cannot be used to measure the TBC accuracy.

The second test case is a more realistic problem arising from geophysics. We study a wave propagating from a point source in a wellbore with fluid surrounded by a VTI homogeneous medium. We consider the same VTI anisotropic medium as in the previous

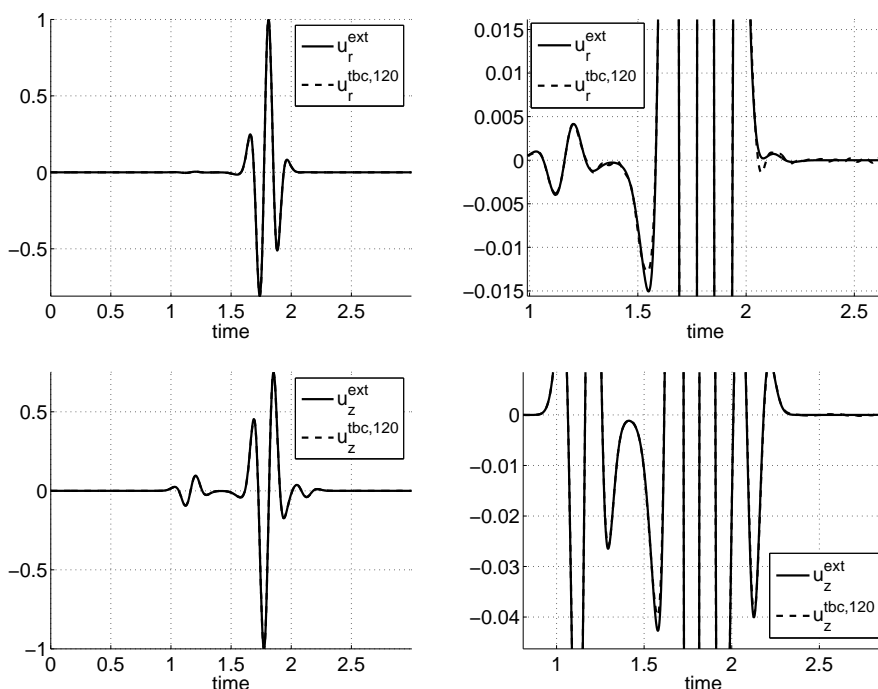


Figure 4: Normalized solution in the receiver at $(0.25, 1.0)$; grid with $h=0.01$, $n_{TBC}=120$. Solid line corresponds to the solution on the extended domain; dashed to the solution to the solution with TBCs. Left: u_r , u_z . Right: zoomed near zero u_r , u_z .

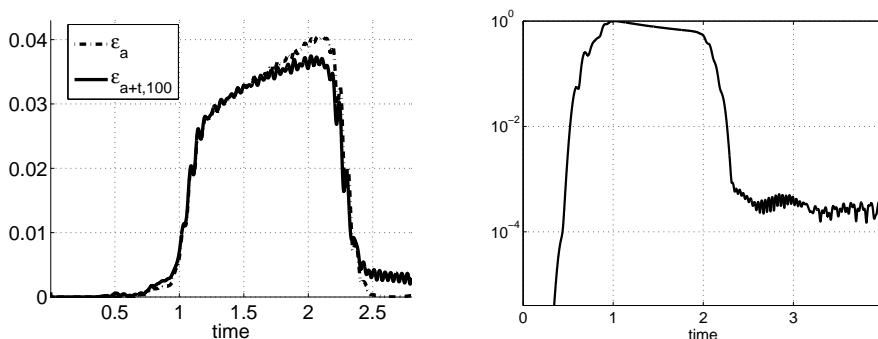


Figure 5: Time dependence of ϵ_a and ϵ_{a+t} for a grid $h=0.01$ and $n_{TBC}=100$ (left). Time dependence of the norm of the solution (right).

case, but keep only the first set of the receivers and increase the central frequency of the source up to 10 (see Fig. 3 (right)). The density of the fluid in the wellbore is $\rho = 1.0$, and the velocity is $V_p = 1.5$; the radius of the wellbore is about 0.1. Numerical results confirm good accuracy of the TBC (see Fig. 6). The error of the TBC, ϵ_t , is about 2% for n_{TBC} greater than 220, that is less than approximation error of the scheme for this problem. Stability of the TBC is checked numerically in long-time simulations (up to $T = 40$).

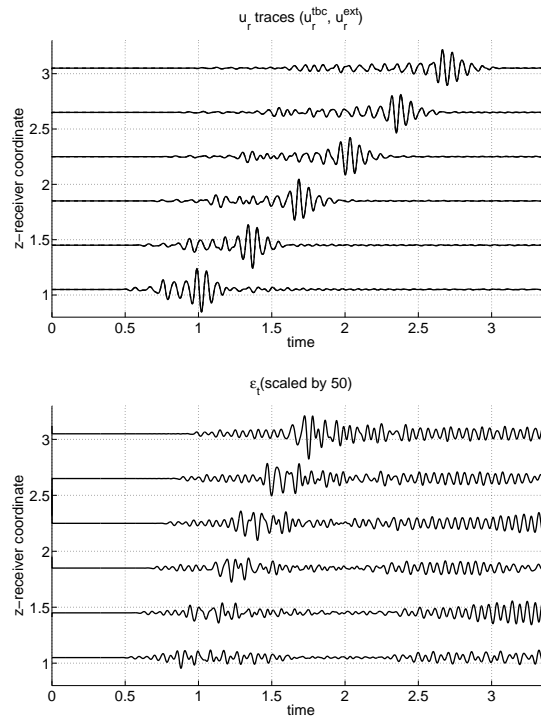


Figure 6: Top: Field u_r in some of the receivers. Two solutions are presented: with TBCs u_r^{tbc} (dashed) and the one obtained on the same grid on the extended domain u_r^{ext} (solid). Bottom: error of TBCs ϵ_t scaled by 50.

7 Conclusions

We have presented the formulation of the transparent boundary condition for elastic anisotropic VTI media for the axially symmetric case and suggested a computationally efficient algorithm for the obtained analytical formulas.

The local part of the TBC can be used as a very fast and easy to implement approximation of the nonreflecting boundary condition, though with limited accuracy. The non-local part, which involves a time convolution, should thus be taken into account if high accuracy is required. We have demonstrated numerically that the convolutional kernel can be approximated by a sum of exponentials and, when the convolution is calculated by recurrence formulas, the computational cost is drastically reduced. In addition speed up is achieved by removing the high-frequency Fourier harmonics from the convolution.

Our TBC representation in terms of the velocity u_r and the stress σ_{rz} facilitates the easy implementation of the TBC into the finite-difference staggered-grid scheme. We have demonstrated high accuracy and stability of the derived TBC for two numerical examples: an academic case with a point source in a homogeneous anisotropic medium (for which PML is unstable) and a realistic case with fluid surrounded by anisotropic medium in a wellbore.

The accuracy of the TBC depends on the accuracy of the approximation of the convolutional kernel and the number of Fourier harmonics included into the non-local part. The desired accuracy level can be reached by increasing the number of exponentials and Fourier harmonics. We use the algorithm [8] for constructing the approximation of the kernel and estimate *a posteriori* accuracy; development of a robust algorithm with guaranteed accuracy is still an open problem.

Acknowledgments

The author is grateful to I. Sofronov for drawing the attention to the considered problem and for stimulating conversations. The author thanks V. Lisitsa, E. Lys, and V. Tcheverda for the forward solver for anisotropic linear elastodynamics based on the finite-difference staggered-grid scheme. The comments of two anonymous reviewers helped improve the manuscript.

References

- [1] B. Alpert, L. Greengard, and T. Hagstrom. Nonreflecting boundary conditions for the time-dependent wave equation. *J. Comput. Phys.*, 180:270–296, 2002.
- [2] E. Becache, S. Fauqueux, and P. Joly. Stability of Perfectly Matched Layers, Group Velocities and Anisotropic Waves, *J. Comput. Phys.*, 188(2):399–433, 2003.
- [3] J.P. Berenger. A perfectly matched layer for the absorption of electromagnetic waves. *J. Comput. Phys.*, 114:185–200, 1994.
- [4] T. Hagstrom, and S. Lau. Radiation boundary conditions for Maxwells equations: A review of accurate time-domain formulations. *J. Comput. Math.*, 25:305–336, 2007.
- [5] V. Lisitsa, and E. Lys. Reflectionless truncation of target area for axially symmetric anisotropic elasticity. *J. Comput. Appl. Math.*, doi:10.1016/j.cam.2009.08.031, 2009
- [6] K.C. Meza-Fajardo and A.S. Papageorgiou. A nonconvolutional, split-field, perfectly matched layer for wave propagation in isotropic and anisotropic elastic media; stability analysis. *Bull. Seism. Soc. Am.*, 98(4):1811–1836, 2008.
- [7] I. Sofronov. Artificial boundary conditions of absolute transparency for two and three-dimensional external time-dependent scattering problems. *Eu. J. Appl. Math.*, 9(6):561–588, 1998.
- [8] I. Sofronov. Nonreflecting inflow and outflow in wind tunnel for transonic time-accurate simulation. *J. Math. Anal. Appl.*, 221:92–115, 1998.
- [9] I.L. Sofronov, and N.A. Zaitsev. Numerical generation of transparent boundary conditions on the side surface of a vertical transverse isotropic layer. *J. Comput. Appl. Math.*, 234:1732–1738, 2010.
- [10] S. Thomsen. Weak elastic anisotropy. *Geophysics*, 51(10):1954–1966, 1986.
- [11] S.V. Tsynkov. Numerical solution of problems on unbounded domains. A review. *Appl. Numer. Math.*, 27(4):465–532, 1998.
- [12] J. Virieux. P-SV wave propagation in heterogeneous media: Velocity-stress finite-difference method. *Geophysics*, 51(4):889–901, 1986.